EQ-INSAR: A Python Package for Generating Synthetic Earthquake InSAR Deformation Data

Konrad Cieslik[1,*] Wojciech Milczarek[2]

[1]trainAI GmbH, Ziegeleiweg 1, 6048 Horw, Switzerland
[2]Department of Geodesy and Geoinformatics, Faculty of Geoengineering Mining and Geology,
Wroclaw University of Science and Technology, Wybrzeże Wyspiańskiego 27, 50-370 Wrocław, Poland

[*]Corresponding author: konrad.cieslik@trainai.io
E-mail: wojciech.milczarek@pwr.edu.pl (W.M.)

February 2026

Abstract

EQ-INSAR is an open-source Python package for generating synthetic Interferometric Synthetic Aperture Radar (InSAR) surface deformation data from earthquake sources. The package implements the Davis (1986) point source model to compute three component ground displacement from double-couple earthquake mechanisms. Then it projects the displacement onto satellite line-of-sight (LOS) geometries to produce interferometric phase maps and binary segmentation labels suitable for machine learning. EQ-INSAR supports 9 pre configured SAR satellite geometries and includes C-band, L-band, and X-band, and provides batch generation of randomized training datasets. Real data validation against the 2021 Yangbi M_w 6.1 earthquake demonstrates subcentimeter RMS fit to observed Sentinel-1 InSAR data and independent recovery of the deformation centroid to within ∼6 km of the Global CMT solution. The software is designed for researchers developing Machine Learning based InSAR analysis tools, educators teaching InSAR interpretation, and scientists requiring synthetic benchmarks for natural and induced seismicity studies.

Keywords: Python, InSAR, earthquake, induced seismicity, synthetic aperture radar, deformation modeling, machine learning, remote sensing

1 Summary

EQ-INSAR incudes three Python APIs for generating synthetic InSAR deformation data from earthquake point sources. The core computation depending only on NumPy:

1. `generate_synthetic_insar()` produces a single interferogram from user specified earthquake parameters (magnitude, strike, dip, rake, depth, satellite), it returs displacement components, LOS displacement, and wrapped/unwrapped phase as NumPy arrays.

2. `generate_timeseries()` creates a multi temporal sequence of pre-event, co-seismic, and post-event frames with binary segmentation labels for supervised learning.

3. `generate_training_batch()` generates N randomized samples and stacks them into (N, T, H, W) arrays which can be used by PyTorch or TensorFlow.

A typical workflow for induced seismicity monitoring might call `generate_training_batch()` to create thousands of synthetic interferograms with user defined magnitude range (M_w 2–5), train a segmentation model on the resulting arrays, and then apply the model to real Sentinel-1 interferograms to flag anomalous deformation patches near injection wells, mining operations or small EQ. Optional dependencies (matplotlib, rasterio, netCDF4) enable visualization and export to GeoTIFF or NetCDF formats.

EQ-INSAR's forward model coupled with standard optimizers can be also use for earthquake source parameter estimation. We demonstrate this capability through real data validation against the 2021 Yangbi M_w 6.1 earthquake (Section 7). It achieved sub centimeter misfit and independent centroid recovery consistent with the Global CMT solution.

2 Statement of Need

Machine learning approaches for InSAR based earthquake detection require large, labeled training datasets [Anantrasirichai et al., 2018, Biggs and Wright, 2020]. Real earthquake InSAR data are limited in availability, expensive to process, and lack pixel level ground truth for supervised learning. Existing deformation modeling tools such as Okada's rectangular dislocation model [Okada, 1985], Pyrocko [Heimann et al., 2017], and Coulomb 3 [Toda et al., 2011] focus on seismological analysis and fault mechanics rather than ML training data generation: they produce raw displacement fields without InSAR specific outputs (LOS projection, phase conversion, wrapped interferograms) or ML utilities (segmentation labels, batch randomization, array stacking).

EQ-INSAR addresses this gap by providing:

- **InSAR native outputs**: LOS displacement, wrapped and unwrapped interferometric phase for any supported satellite geometry.
- **Machine Learning ready labels**: Binary segmentation masks with configurable displacement thresholds.
- **Time series structure**: Pre-event, co-seismic, and post-event frames for temporal models.
- **Batch generation**: Randomized earthquake parameters and noise levels producing stacked arrays in (N, T, H, W) format, directly compatible with PyTorch and TensorFlow.

The underlying point source model is well suited for small to moderate earthquakes ($M_w \lesssim 6.5$). This makes EQ-INSAR particularly applicable to induced seismicity from mining, hydraulic fracturing, wastewater injection, and geothermal operations. Those events are typically $M_w < 5$ and well within the point source validity range [Ellsworth, 2013]. InSAR monitoring of induced seismicity is a growing field where ML based detection can complement sparse seismic networks [Milczarek et al., 2021, Cieślik et al., 2024], and EQ-INSAR enables rapid generation of realistic training data for these scenarios.

3 Method

EQ-INSAR's forward model proceeds in four stages: (1) earthquake source parameterization, (2) elastic half-space displacement, (3) LOS projection, and (4) phase conversion. Each stage is described below.

3.1 Earthquake source parameterization

The earthquake source is specified by moment magnitude M_w, fault geometry (strike ϕ_s, dip δ, rake λ), and hypocentral depth d. The scalar seismic moment M_0 is obtained from the Hanks & Kanamori (1979) relation [Hanks and Kanamori, 1979]:

$$\log_{10} M_0 = 1.5\, M_w + 9.1 \quad (M_0 \text{ in N m}). \tag{1}$$

The double-couple moment tensor is constructed following the Aki & Richards (2002) convention [Aki and Richards, 2002]. Given the fault normal vector $\hat{\mathbf{n}}$ and slip vector $\hat{\mathbf{s}}$ (both derived from strike, dip, and rake in the East-North-Up coordinate system), the moment tensor is:

$$\mathbf{M} = M_0 \left(\hat{\mathbf{s}} \otimes \hat{\mathbf{n}} + \hat{\mathbf{n}} \otimes \hat{\mathbf{s}} \right), \tag{2}$$

yielding six independent components M_{ee}, M_{nn}, M_{uu}, M_{en}, M_{nu}, M_{ue} with zero trace.

3.2 Elastic half-space displacement

Surface displacement is computed using the Davis (1986) analytical Green's functions for a point moment tensor source in a homogeneous, isotropic elastic half-space [Davis, 1986]. For a source at depth d and an observation point at horizontal offset (x_1, x_2) from the epicenter, the distance is $R = \sqrt{x_1^2 + x_2^2 + d^2}$. The displacement field for each moment tensor component M_{ij} is expressed through auxiliary coefficients:

$$\alpha = \frac{3R + d}{R^3 (R + d)^3}, \quad \beta = \frac{2R + d}{R^3 (R + d)^2}, \quad \eta = \frac{1}{R (R + d)^2}, \quad \psi = \frac{1}{R (R + d)}, \tag{3}$$

which enter Green's functions $G_k^{ij}(x_1, x_2, d)$ relating moment tensor component M_{ij} to displacement component $k \in \{e, n, u\}$. The total surface displacement is:

$$U_k = \frac{1}{2\pi\mu} \sum_{i,j} M_{ij}\, G_k^{ij}(x_1, x_2, d), \tag{4}$$

where μ is the shear modulus (default: 30 GPa) and ν is Poisson's ratio (default: 0.25). The parameter $\bar{\nu} = 1 - 2\nu$ appears in the Green's function expressions. The full Green's function expressions for all six moment tensor components are implemented following Davis [1986]; the complete expressions are documented in the package source code.

3.3 LOS projection

The three component displacement vector $\mathbf{U} = (U_e, U_n, U_u)$ is projected onto the satellite line-of-sight (LOS) direction. The LOS unit vector pointing from the ground to the satellite is:

$$\hat{\mathbf{l}} = \begin{pmatrix} -\sin\theta \, \sin\alpha_h \\ \sin\theta \, \cos\alpha_h \\ \cos\theta \end{pmatrix}, \tag{5}$$

where θ is the incidence angle (from vertical) and α_h is the satellite heading azimuth (from North, clockwise). The LOS displacement is the dot product:

$$d_{\text{LOS}} = \hat{\mathbf{l}} \cdot \mathbf{U} = U_e\, l_e + U_n\, l_n + U_u\, l_u, \tag{6}$$

where positive d_{LOS} indicates motion toward the satellite (range decrease).

3.4 Phase conversion and noise

The LOS displacement is converted to interferometric phase via the two way path relation:

$$\varphi = -\frac{4\pi}{\lambda} d_{\mathrm{LOS}}, \tag{7}$$

where λ is the radar wavelength (e.g., 5.55 cm for Sentinel-1 C-band). Wrapped phase is obtained by mapping φ to the $[-\pi, \pi]$ interval. Optional additive Gaussian noise $\mathcal{N}(0, \sigma^2)$ and linear orbital ramp errors can be applied to simulate measurement noise.

4 Verification

We verify EQ-INSAR's implementation through two consistency checks, each exercising a different analytical property of the Davis (1986) point source model. All tests were run with $M_w = 6.0$ ($M_0 = 1.259 \times 10^{18}$ N m).

Symmetry of displacement patterns. The Green's functions possess symmetries determined by the source mechanism. We test three cases on a 201×201 grid (± 50 km, depth = 10 km):

1. *Isotropic source* ($M_{ee} = M_{nn} = M_{uu} = M_0/3$): U_u must be radially symmetric. All mirror and transpose tests yield exactly zero difference (to floating-point precision).

2. *Strike-slip* (strike = 0°, dip = 90°, rake = 0°): U_u must be antisymmetric about both the EW and NS axes. Measured maximum relative residuals are $< 6 \times 10^{-16}$.

3. *Dip-slip* (strike = 0°, dip = 90°, rake = 90°): U_u must be symmetric about the EW axis (the fault strike direction). Measured maximum relative residual is 2.4×10^{-16}.

All symmetry tests pass to within machine precision ($\sim 10^{-16}$ relative).

Moment tensor zero-trace property. A pure double-couple source must satisfy $\mathrm{tr}(\mathbf{M}) = M_{ee} + M_{nn} + M_{uu} = 0$. We evaluate 10,000 random fault orientations with strike $\in [0°, 360°)$, dip $\in [0°, 90°]$, and rake $\in [-180°, 180°]$. The maximum observed $|\mathrm{tr}(\mathbf{M})|/M_0 = 5.1 \times 10^{-16}$, confirming the zero-trace property to machine precision in all cases.

Far-field $1/d^2$ displacement decay. For a point source, the peak surface displacement must scale as $U_u^{\max} \propto d^{-2}$ where d is the source depth. We compute the peak vertical displacement for a thrust earthquake (strike = 45°, dip = 30°, rake = 90°) at depths of 5, 10, 20, 40, and 80 km (grid: 401×401 points, extent = $10 \times d$). Table 1 shows the results: the product $|U_u^{\max}| \times d^2$ is constant across all depths, and a loglog linear regression yields a slope of -2.000 with $R^2 = 1.000$, confirming exact $1/d^2$ scaling.

Table 1: Peak vertical displacement versus source depth for M_w 6.0 thrust source, verifying $1/d^2$ decay.

Depth (km)	Peak $\lvert U_u \rvert$ (m)	$\lvert U_u \rvert \times d^2$	Ratio to $d = 5$ km
5	4.061×10^{-1}	1.015×10^{7}	1.000000
10	1.015×10^{-1}	1.015×10^{7}	1.000000
20	2.538×10^{-2}	1.015×10^{7}	1.000000
40	6.345×10^{-3}	1.015×10^{7}	1.000000
80	1.586×10^{-3}	1.015×10^{7}	1.000000

These checks confirm that the implementation correctly reproduces the analytical properties of the Davis (1986) point source model. The point source approximation is well established for earthquakes where the fault dimension is small relative to the source depth and observation distance, a condition typically satisfied for $M_w \lesssim 6.5$ [Davis, 1986, Okada, 1985].

5 Key Features

EQ-INSAR provides three generator functions:

```
from eq_insar import (generate_synthetic_insar,
    generate_timeseries, generate_training_batch,
    batch_to_arrays)

# Single interferogram for Mw 6.0 thrust earthquake
result = generate_synthetic_insar(
    Mw=6.0, strike_deg=45, dip_deg=30, rake_deg=90,
    depth_km=10, satellite='sentinel1'
)

# Time series with pre/co/post-event frames
ts = generate_timeseries(Mw=6.0, n_pre=5, n_event=1, n_post=5)

# Batch of 100 samples -> stacked arrays (N, T, H, W)
batch = generate_training_batch(n_samples=100, mw_range=(5.0, 7.0))
X, y = batch_to_arrays(batch)['X'], batch_to_arrays(batch)['y']
```

Each generator returns displacement components (U_e, U_n, U_z), LOS displacement, phase products, and metadata. The `batch_to_arrays` helper stacks batch output into NumPy arrays in (N, T, H, W) format, where N is the number of samples, T is the number of time steps (pre-event + co-seismic + post-event frames, serving as the channel dimension), and $H \times W$ is the spatial grid. This maps directly to PyTorch's channels-first convention (N, C, H, W); for TensorFlow's channels-last convention, a simple transpose converts to (N, H, W, T).

Figure 1 shows displacement components and InSAR products for an M_w 6.0 thrust earthquake.

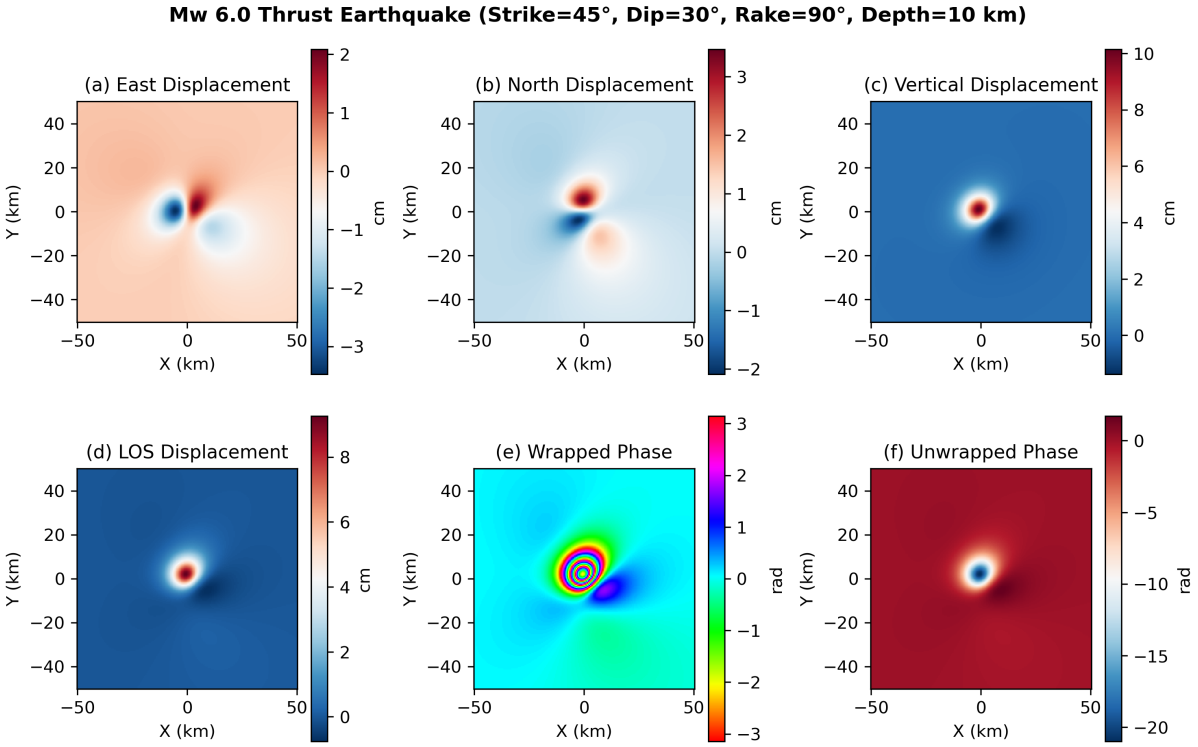

Figure 1: Displacement components and InSAR products for a synthetic M_w 6.0 thrust earthquake (strike = 45°, dip = 30°, rake = 90°, depth = 10 km) with Sentinel-1 ascending geometry. Top row: East, North, and vertical displacement. Bottom row: LOS displacement, wrapped phase, and unwrapped phase.

Figure 2 compares LOS displacement and wrapped phase for thrust, normal, and strike-slip mechanisms, illustrating the distinct fringe patterns produced by each fault type.

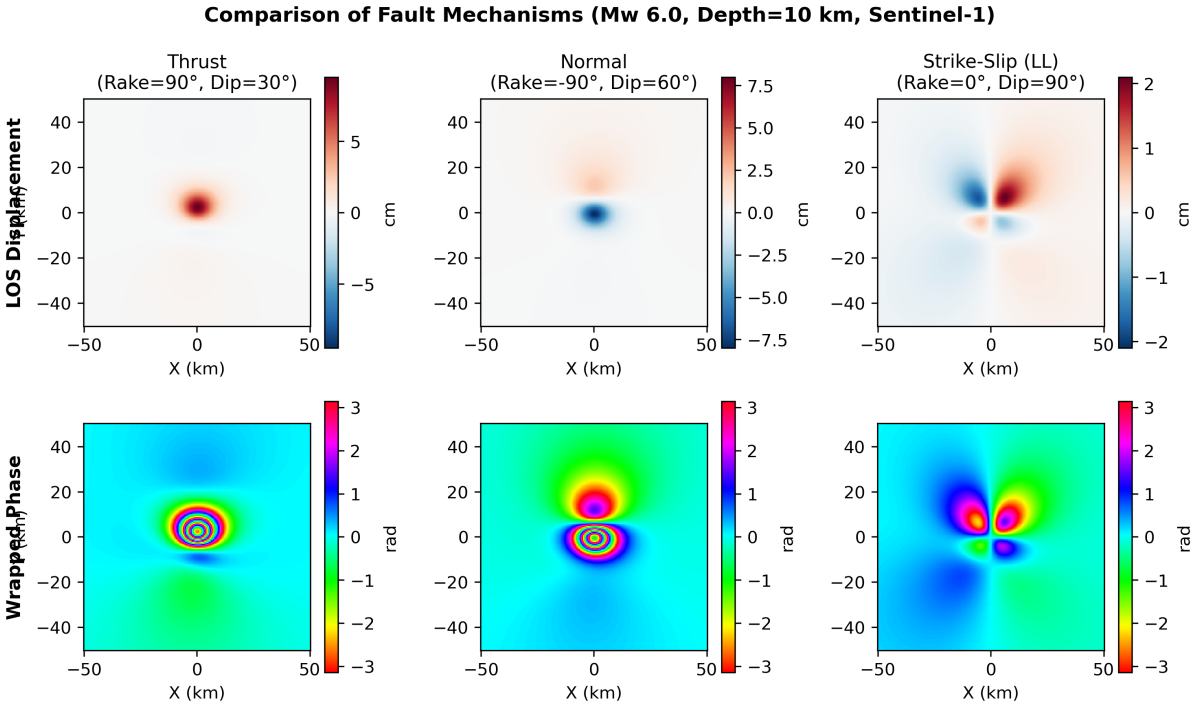

Figure 2: Synthetic interferograms for three fault mechanisms: thrust (rake = 90°), normal (rake = −90°), and strike-slip (rake = 0°). Top: LOS displacement. Bottom: wrapped phase.

The time series generator produces temporal frames with binary segmentation labels (Figure 3).

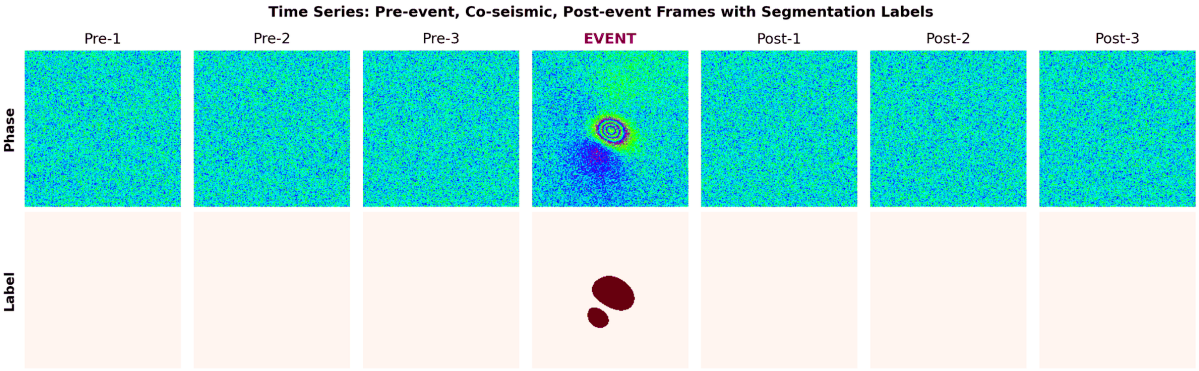

Figure 3: Time series: pre-event frames (noise only, no deformation signal), co-seismic event (signal + noise), post-event frames (noise only), with binary segmentation labels. Color scales are shared across all frames.

The `generate_training_batch` function creates diverse samples with randomized parameters (Figure 4).

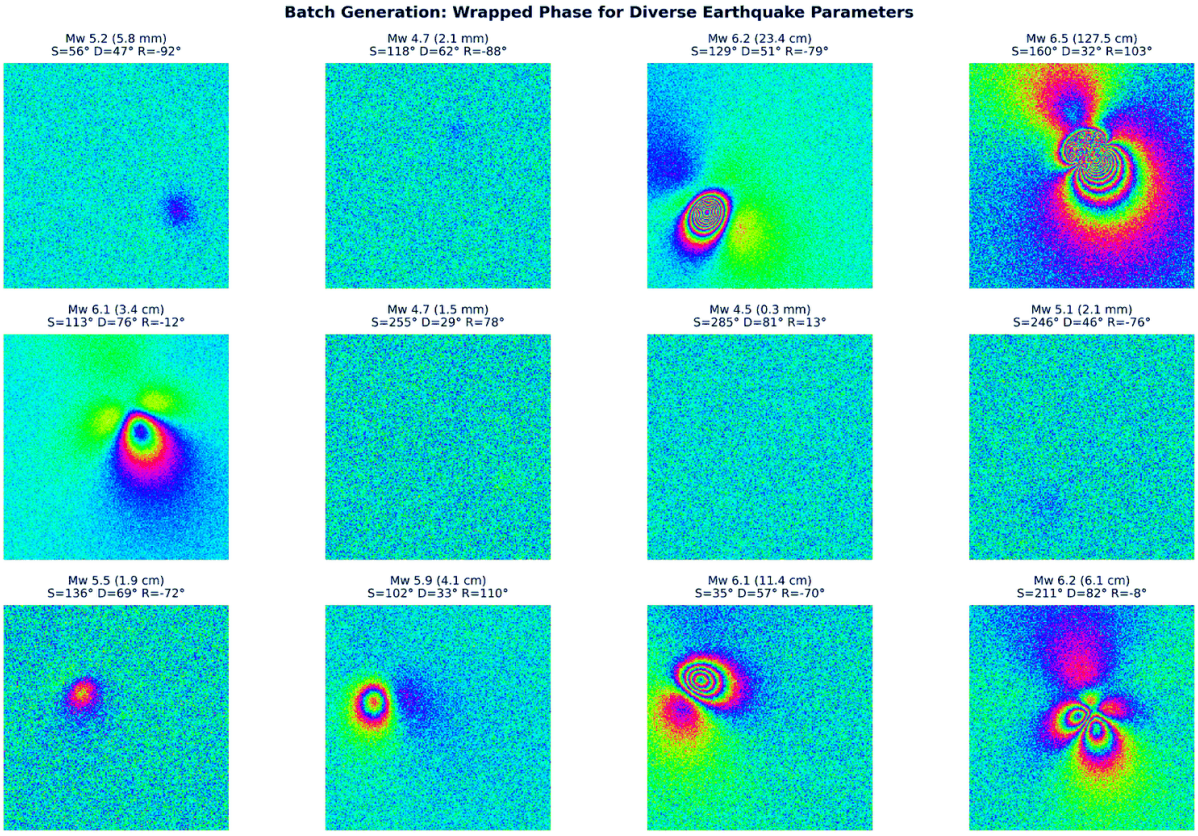

Figure 4: Batch-generated samples showing wrapped phase for earthquakes with varying magnitude, depth, and fault orientation. Note that color scales differ between panels due to the different earthquake parameters.

6 Related Software

Several tools exist for modeling earthquake surface deformation (Table 2). Okada's (1985) rectangular dislocation model [Okada, 1985] is the standard for finite fault inversions and is implemented in numerous languages, but produces raw displacement without InSAR-specific outputs or ML utilities. Pyrocko [Heimann et al., 2017] is a comprehensive seismology toolbox offering Green's function databases and moment tensor analysis, oriented toward seismological research rather than synthetic data generation. Coulomb 3 [Toda et al., 2011] computes stress changes and displacement on receiver faults, primarily for Coulomb failure analysis. EQ-INSAR differs from these tools by combining the forward deformation model with InSAR observation geometry, phase conversion, noise simulation, and Machine Learning oriented batch generation in a single lightweight package.

Table 2: Feature comparison of deformation modeling tools. Multi-satellite support† is a convenience feature (pre-configured orbital parameters); LOS projection can be applied manually to any displacement field.

Feature	EQ-INSAR	Okada	Pyrocko	Coulomb 3
Point source model	✓	–	✓	–
Finite fault model	–	✓	✓	✓
Layered earth model	–	–	✓	–
Waveform modeling	–	–	✓	–
LOS displacement	✓	–	✓*	–
Interferometric phase	✓	–	–	–
Multi-satellite support†	✓	–	–	–
Segmentation labels	✓	–	–	–
Time series generation	✓	–	–	–
Batch randomization	✓	–	–	–
Stress analysis	–	–	–	✓
Coulomb failure analysis	–	–	–	✓

*Via the Kite companion library [Heimann et al., 2017].
†Pre-configured orbital parameters for 9 SAR satellites.

7 Real-Data Validation

To demonstrate EQ-INSAR's applicability to real earthquake observations, we perform a source parameter inversion for the 2021 Yangbi M_w 6.1 earthquake (Yunnan, China). The initial source parameters (strike = 135°, dip = 82°, rake = −165°, depth = km) and hypocenter location (25.727°N, 100.008°E) were obtained from the USGS catalog [U.S. Geological Survey, 2021]. The coseismic Sentinel-1 ascending LOS displacement field was obtained from the InSAR dataset of Liu et al. [2022]. We invert for seven parameters: M_w, strike, dip, rake, depth, and epicenter offset (x_{cen}, y_{cen}) by minimizing the root mean square (RMS) misfit between the observed LOS displacement and EQ-INSAR forward model predictions using the `differential_evolution` global optimizer from SciPy.

Table 3 summarizes the inversion results. To illustrate the need for inversion, Figure 5b shows the forward model using the USGS catalog parameters with the epicenter as the deformation center, the predicted displacement pattern is centered on the wrong location and poorly matches the observed field (RMS = 2.0 cm). The optimizer reduces the RMS misfit to 0.86 cm (Figure 5e), a 57% improvement, primarily by relocating the deformation centroid. The inverted strike (149.3°) and dip (85.4°) are consistent with the catalog values and with published InSAR studies reporting strikes of 135–141° and near-vertical dip angles [Liu et al., 2022]. The magnitude (M_w 6.03) and depth (8.6 km) are also consistent with the catalog values. The inverted rake (−124°) shows a larger normal faulting component than the catalog (−165°).

The bigest difference which the inversion provided isepicenter offsets of $x_{\text{cen}} = -6.2$ km (west) and $y_{\text{cen}} = -11.9$ km (south) relative to the USGS teleseismic hypocenter [U.S. Geological Survey, 2021]. Our inversion relocated the deformation centroid to approximately 25.62°N, 99.95°E, a shift of ∼13 km (Fig. 5f). This relocation is independently checked by the Global Centroid Moment Tensor (GCMT) solution [Ekström et al., 2021], which places the centroid at 25.62°N, 100.01°E, only ∼6 km from the EQ-INSAR result. Figure 5f compares locations from multiple agencies retrieved from their respective online catalogs: the USGS [U.S. Geological Survey, 2021] and ISC [International Seismological Centre, 2021] teleseismic hypocenters cluster ∼11–13 km north of the EQ-INSAR centroid, reflecting the well-known mislocation bias of teleseismic solutions, while the GCMT centroid [Ekström et al., 2021], which represents the spatial centroid of moment release rather than the rupture nucleation point lies much closer to the EQ-INSAR estimate. This demonstrates that the EQ-INSAR point source inversion inde-

pendently recovers the deformation centroid consistent with the GCMT solution, using only a single ascending InSAR displacement field.

Table 3: Source parameter inversion results for the 2021 Yangbi (China) M_w 6.1 earthquake. Catalog parameters from the USGS focal mechanism; inverted parameters from constrained differential evolution optimization (±25% on focal mechanism, free location) of ascending Sentinel-1 LOS displacement. Offsets x_{cen} (east) and y_{cen} (north) are relative to the USGS teleseismic epicenter (25.727°N, 100.008°E).

Source	M_w	Strike (°)	Dip (°)	Rake (°)	Depth (km)	x_{cen} (km)	y_{cen} (km)	RMS (cm)
Catalog	6.10	135.0	82.0	−165.0	9.0	0.0	0.0	2.0
Inverted	6.03	149.3	85.4	−123.8	8.58	−6.2	−11.9	0.86

Figure 5 compares the observed ascending LOS displacement (a), the catalog forward model (b), and the inverted synthetic (c), with corresponding residuals (d, e). The catalog forward model, centered at the USGS teleseismic epicenter, visibly mislocates the deformation pattern, while the inverted synthetic captures the bilateral pattern characteristic of strike-slip faulting with residuals below 1 cm RMS.

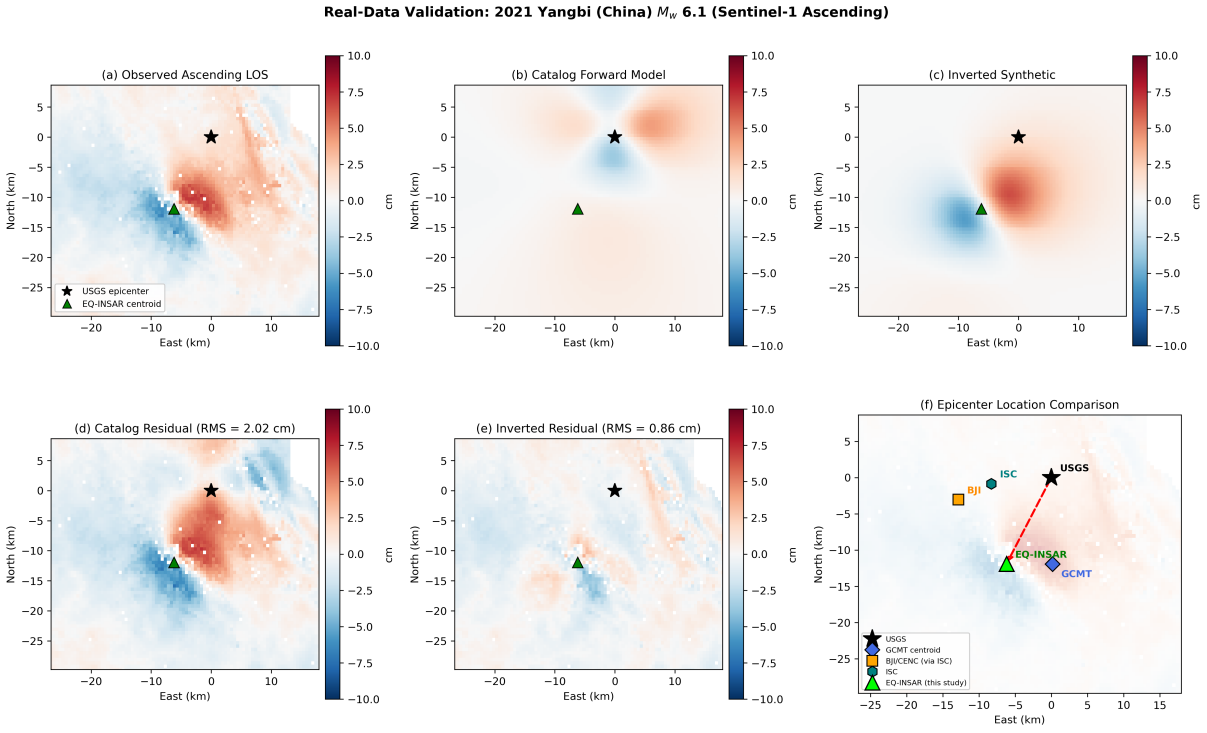

Figure 5: Real-data validation: 2021 Yangbi (China) M_w 6.1 earthquake. (a) Observed Sentinel-1 ascending LOS displacement. (b) Forward model using USGS catalog parameters centered at the teleseismic epicenter. (c) Inverted synthetic from EQ-INSAR point source model with optimized parameters. (d) Catalog residual (RMS = 2.02 cm). (e) Inverted residual (RMS = 0.86 cm). (f) Epicenter location comparison from online catalogs: USGS teleseismic hypocenter (black star), GCMT centroid (blue diamond), BJI/CENC via ISC (orange square), ISC (teal hexagon), and EQ-INSAR inverted centroid (green triangle). The red dashed arrow shows the ∼13 km relocation from the USGS hypocenter to the EQ-INSAR solution, which lies within ∼6 km of the independently determined GCMT centroid. Color scale in centimeters.

This example demonstrates that EQ-INSAR, produces displacement fields that are quan-

titatively comparable to real InSAR observations for moderate earthquakes. The ability to independently recover the deformation centroid to within ∼6 km of the GCMT solution, and to correct teleseismic mislocation by ∼13 km highlights the package's potential not only for synthetic training data generation but also for rapid source parameter estimation and earthquake relocation using InSAR data.

8 Limitations

- **Point source approximation**: Appropriate for earthquakes where the fault dimension is small relative to the source depth ($L, W \ll d$) / earthquakes with magnitudes smaller than 6.5. For larger earthquakes, finite fault models [Okada, 1985] provide more accurate displacement patterns.
- **Homogeneous elastic half-space**: The model assumes laterally homogeneous elastic properties. Crustal layering, lateral heterogeneity, and material contrasts across fault zones are not modeled.
- **No topographic correction**: The free surface is assumed flat. Topographic phase contributions and geometric distortions (layover, foreshortening) in mountainous terrain are not accounted for.

9 Code and Data Availability

EQ-INSAR is open-source software released under the MIT License (version 0.1.0) [Cieslik and Milczarek, 2026]. The source code, documentation, examples, and test suite are available at `https://github.com/kcieslik/eq-insar`. An archived release is deposited on Zenodo with DOI: 10.5281/zenodo.18647189. The package can be installed with `pip install eq-insar` and requires Python ≥ 3.8. The core functionality depends only on NumPy; matplotlib, rasterio, and netCDF4 are optional dependencies for visualization and I/O. The test suite (`pytest tests/`) verifies the symmetry and decay reported in Section 4.

Acknowledgements

The authors thank the open-source community for NumPy [Harris et al., 2020], SciPy [Virtanen et al., 2020], and Matplotlib [Hunter, 2007].

References

Keiiti Aki and Paul G. Richards. *Quantitative Seismology*. University Science Books, Sausalito, California, 2nd edition, 2002. ISBN 0-935702-96-2.

Nantheera Anantrasirichai, Juliet Biggs, Fabien Albino, Peter Hill, and David Bull. Application of machine learning to classification of volcanic deformation in routinely generated InSAR data. *Journal of Geophysical Research: Solid Earth*, 123(8):6592–6606, 2018. doi: 10.1029/2018JB015911.

Juliet Biggs and Tim J. Wright. How satellite insar has grown from opportunistic science to routine monitoring over the last decade. *Nature Communications*, 11(1):3863, 2020. doi: 10.1038/s41467-020-17587-6.

Konrad Cieslik and Wojciech Milczarek. Eq-insar: A python package for generating synthetic earthquake insar deformation data, 2026. URL `https://github.com/kcieslik/eq-insar`.

Konrad Cieślik, Wojciech Milczarek, Ewa Warchala, Paweł Kosydor, and Robert Rożek. Identifying factors influencing surface deformations from underground mining using sar data, machine learning, and the shap method. *Remote Sensing*, 16(13):2428, 2024. doi: 10.3390/rs16132428.

Paul M. Davis. Surface deformation due to inflation of an arbitrarily oriented triaxial ellipsoidal cavity in an elastic half-space, with reference to Kilauea volcano, Hawaii. *Journal of Geophysical Research: Solid Earth*, 91(B7):7429–7438, 1986. doi: 10.1029/JB091iB07p07429.

Göran Ekström, Meredith Nettles, and Adam M. Dziewoński. Global CMT catalog event C202105211348A, 2021. URL https://www.ldeo.columbia.edu/~gcmt/projects/CMT/catalog/NEW_MONTHLY/2021/may21.ndk. Accessed 2026-02-23.

William L. Ellsworth. Injection-induced earthquakes. *Science*, 341(6142):1225942, 2013. doi: 10.1126/science.1225942.

Thomas C. Hanks and Hiroo Kanamori. A moment magnitude scale. *Journal of Geophysical Research: Solid Earth*, 84(B5):2348–2350, 1979. doi: 10.1029/JB084iB05p02348.

Charles R. Harris, K. Jarrod Millman, Stéfan J. van der Walt, Ralf Gommers, Pauli Virtanen, David Cournapeau, Eric Wieser, Julian Taylor, Sebastian Berg, Nathaniel J. Smith, Robert Kern, Matti Picus, Stephan Hoyer, Maarten H. van Krevelen, Matthew Brett, Allan Haldane, Jaime Fernández del Río, Mark Wiebe, Pearu Peterson, Pierre Gérard-Marchant, Kevin Sheppard, Tyler Reddy, Warren Weckesser, Hameer Abbasi, Christoph Gohlke, and Travis E. Oliphant. Array programming with NumPy. *Nature*, 585(7825):357–362, 2020. doi: 10.1038/s41586-020-2649-2.

Sebastian Heimann, Marius Kriegerowski, Marius Isken, Simone Cesca, Simon Daout, Francesco Grigoli, Carina Juretzek, Tobias Megies, Nima Nooshiri, Andreas Steinberg, Henriette Sudhaus, Hannes Vasyura-Bathke, Timothy Willey, and Torsten Dahm. Pyrocko - an open-source seismology toolbox and library. *GFZ Data Services*, 2017. doi: 10.5880/GFZ.2.1.2017.001.

John D. Hunter. Matplotlib: A 2d graphics environment. *Computing in Science & Engineering*, 9(3):90–95, 2007. doi: 10.1109/MCSE.2007.55.

International Seismological Centre. ISC bulletin: Event 619523040, 2021. URL https://www.isc.ac.uk/iscbulletin/search/bulletin/. Accessed 2026-02-23.

Xiaoge Liu, Wenbin Xu, Zhiguo He, Lihua Fang, and Lichun Chen. Aseismic slip and cascade triggering process of foreshocks leading to the 2021 m_w 6.1 Yangbi earthquake. *Seismological Research Letters*, 93(3):1413–1428, 2022. doi: 10.1785/0220210263.

Wojciech Milczarek, Anna Kopeć, Dariusz Głąbicki, and Natalia Bugajska. Induced seismic events—distribution of ground surface displacements based on insar methods and mogi and yang models. *Remote Sensing*, 13(8):1451, 2021. doi: 10.3390/rs13081451.

Yoshimitsu Okada. Surface deformation due to shear and tensile faults in a half-space. *Bulletin of the Seismological Society of America*, 75(4):1135–1154, 1985. doi: 10.1785/BSSA0750041135.

Shinji Toda, Ross S. Stein, Volkan Sevilgen, and Jian Lin. Coulomb 3.3 graphic-rich deformation and stress-change software for earthquake, tectonic, and volcano research and teaching—user guide. *U.S. Geological Survey Open-File Report*, 2011-1060:63, 2011. doi: 10.3133/ofr20111060.

U.S. Geological Survey. M 6.1 – 25 km NW of Dali, China (event us7000e532), 2021. URL https://earthquake.usgs.gov/earthquakes/eventpage/us7000e532. Accessed 2026-02-23.

Pauli Virtanen, Ralf Gommers, Travis E. Oliphant, Matt Haberland, Tyler Reddy, David Cournapeau, Evgeni Burovski, Pearu Peterson, Warren Weckesser, Jonathan Bright, Stéfan J. van der Walt, Matthew Brett, Joshua Wilson, K. Jarrod Millman, Nikolay Mayorov, Andrew R. J. Nelson, Eric Jones, Robert Kern, Eric Larson, C J Carey, İlhan Polat, Yu Feng, Eric W. Moore, Jake VanderPlas, Denis Laxalde, Josef Perktold, Robert Cimrman, Ian Henriksen, E. A. Quintero, Charles R. Harris, Anne M. Archibald, Antônio H. Ribeiro, Fabian Pedregosa, Paul van Mulbregt, and SciPy 1.0 Contributors. SciPy 1.0: Fundamental algorithms for scientific computing in Python. *Nature Methods*, 17:261–272, 2020. doi: 10.1038/s41592-019-0686-2.